

Article

A Four-Band Terahertz Metamaterial Sensor Based on Symmetric E-Shaped Structure

Li Li ^{1,2,3}, Hongyi Ge ^{1,2,3,*}, Yuying Jiang ^{1,2,4,*} , Guangming Li ^{1,2,3}, Fei Wang ^{1,2,3}, Ming Lv ^{1,2,3} , Xiaodi Ji ^{1,2,3}, Zhiyuan Jia ^{1,2,3}, Zhi Li ^{1,2,3} and Yuan Zhang ^{1,2,*}

- ¹ Key Laboratory of Grain Information Processing and Control, Ministry of Education, Henan University of Technology, Zhengzhou 450001, China
² Henan Provincial Key Laboratory of Grain Photoelectric Detection and Control, Henan University of Technology, Zhengzhou 450001, China
³ College of Information Science and Engineering, Henan University of Technology, Zhengzhou 450001, China
⁴ School of Artificial Intelligence and Big Data, Optics, Henan University of Technology, Zhengzhou 450001, China
* Correspondence: gehongyi2004@163.com (H.G.); jiangyuying11@163.com (Y.J.); zy_haut@163.com (Y.Z.)

Abstract: To realize the multi-frequency selectivity of the analyte, a novel four-band terahertz metamaterial sensor is proposed in this work. In particular, the sensor performance is analyzed theoretically and numerically within a terahertz frequency range (0.8–1.5 THz) via the finite element method. According to the results, higher-order Fano resonance is the main cause of the four narrow and sharp transmission valleys in the operating band region of the sensor, yielding high resolution with Q values up to 177. Moreover, this sensor is polarization-insensitive over a wide polarization angle range of 0° to 50°. In addition, the sensor achieves refractive index sensitivity of 200 GHz/RIU and offers FOM values of up to 26.7. The sensor proposed in this study exhibits a simple structure, frequency selection characteristics, low cost, and enhances the interaction between terahertz waves and substances, which is of great theoretical and practical significance for the development of terahertz functional devices such as sensors and filters.

Keywords: terahertz; two-dimensional materials; metamaterials; sensor; Q-factor



Citation: Li, L.; Ge, H.; Jiang, Y.; Li, G.; Wang, F.; Lv, M.; Ji, X.; Jia, Z.; Li, Z.; Zhang, Y. A Four-Band Terahertz Metamaterial Sensor Based on Symmetric E-Shaped Structure.

Coatings **2022**, *12*, 1694. <https://doi.org/10.3390/coatings12111694>

Academic Editors: Devis Bellucci and Anton Ficai

Received: 18 September 2022

Accepted: 31 October 2022

Published: 7 November 2022

Publisher's Note: MDPI stays neutral with regard to jurisdictional claims in published maps and institutional affiliations.



Copyright: © 2022 by the authors. Licensee MDPI, Basel, Switzerland. This article is an open access article distributed under the terms and conditions of the Creative Commons Attribution (CC BY) license (<https://creativecommons.org/licenses/by/4.0/>).

1. Introduction

Terahertz (THz) technology, as a new type of detection method, has been widely used in non-destructive testing, quality control, and safety screening in biomedical tissues, agricultural products, and other fields [1–3]. This is because the terahertz band recognizes the spatial conformation of biomolecular functions that cannot be detected by other electromagnetic bands [4]. As a result, the structure and physical properties of substances can be analyzed and identified through characteristic frequencies. At the same time, the comparatively low photon energy of terahertz waves, when penetrating substances, does not damage biological tissues due to ionization [5]. Shao successfully applied the partial least squares algorithm in terahertz data modeling to distinguish between various lipid contents of *S. obliquus* [6]. Im investigated terahertz optical properties in the content of an effective medium model to pave the way for real-time monitoring of microplastics in salt [7]. Zhu combined terahertz time-domain spectroscopy (THz-TDS) and density functional theory to realize the detection of proline, hydroxyproline, and pyroglutamic acid [8]. Lee proposed a method to determine the concentrations of monosaccharides in the atmosphere using reconstructed signals [9]. Jiang developed a boosting-based multi-variate data fusion approach for quantitative detection of wheat maltose [10]. Meanwhile, even though great progress has been made in detection techniques, substances still exhibit strong absorption and dispersion properties in the terahertz band range. This weakens

the interaction between the free-space propagating terahertz waves and the substance's structure, which inhibits the detection at the micro or trace level.

Metamaterials (MMs) have been opening the door to the rapid development of THz technology [11,12]. MMs are capable of achieving flexible and diverse control over the amplitude [13], phase [14], and propagation [15] of terahertz waves, which compensates to a certain extent for the rigid problems of THz-TDS technology. Terahertz metamaterial sensors are the label-free, affinity-type sensors that are extremely sensitive to changes in surface dielectric constants. In this respect, the advantages of combining the local electromagnetic field enhancement of metamaterials with the THz waves in detectors have attracted widespread attention. For instance, Yang, Cheng, and Zhang et al. used terahertz metamaterial sensors to identify various cancer cells, proteins, and other substances, extending the capabilities of metamaterials in the bio-detection [16–21]. Tantiwanichapan, Du, and other research teams have conducted research in the detection of pesticide residues, which has laid the foundation for ensuring the quality and safety of food and agricultural products [22–26]. Xu, Li et al. could distinguish between different solutions, showing the potential of terahertz sensors for chemical and related fields of applications [27–29].

Until now, various attempts have been made to obtain electromagnetic resonance-enhanced responses in enhanced terahertz sensing by using metallic micro-structured metamaterials. Unfortunately, while single or dual resonance peaks are commonly used for sensing and detection in the terahertz band region, the reports on multi-peak sensors are still scarce, which greatly limits the application prospects of terahertz sensors. Besides, multi-peak resonators usually require a complex structural design that is hard to realize [30]. Moreover, various scholars, in pursuit of higher sensitivity, offer sensors that often operate at frequencies beyond the existing THz-TDS working bandwidth, which is not suitable in practical detection [31]. In addition, most of the research achievements only analyze the refractive index sensitivity of the sensors, yet few of them are reported for the thickness sensitivity [32].

In view of this, a structurally simple y -axis symmetric terahertz metamaterial sensor is proposed in this work to achieve four-band filtered resonance performance within a frequency range from 0.8 to 1.5 THz. The metamaterial structural unit is a subwavelength element to build a near-infinite periodic array. The physical mechanism of resonance phenomena of the sensor is explored by analyzing the near-field distribution of the sensor at the resonance frequency. In particular, the polarization-sensitive characteristics of the sensor are investigated at different incident angles and polarization angles of the electromagnetic wave. Moreover, the sensing performance of the sensor is evaluated based on the theoretical values of the thickness and refractive index of the biological sample. The sensor designed in this work is easy to fabricate and differs from the conventional filtrate-type sensors, opening up new prospects in terahertz waves' control for sensing, filters, and other technology-related fields.

2. Design and Simulation

Figure 1 shows the structural unit of the designed terahertz metamaterial sensor. As can be seen in Figure 1a, the structural unit consists of a metal microstructure resonance layer and a dielectric substrate layer. Due to the many features of flexible substrates such as flexibility, portability, low cost, and biocompatibility, the dielectric layer is made of polyimide (PI), a flexible material with a dielectric constant $\epsilon = 3.5 + i0.0027$, and has the thickness $h = 60 \mu\text{m}$. The metallic microstructure layer is capable of interacting strongly with the incident electromagnetic waves. The physical properties of gold are stable and not easily oxidized and corroded by the atmosphere. In this paper, gold with conductivity $\sigma_{\text{Au}} = 4.561e + 007 \text{ S/m}$ is used as the resonance structure material with thickness $t = 0.2 \mu\text{m}$. More information about the dimensional parameters of the optimized unit structure, enabling one to achieve multi-band transmission, can be found in Table 1.

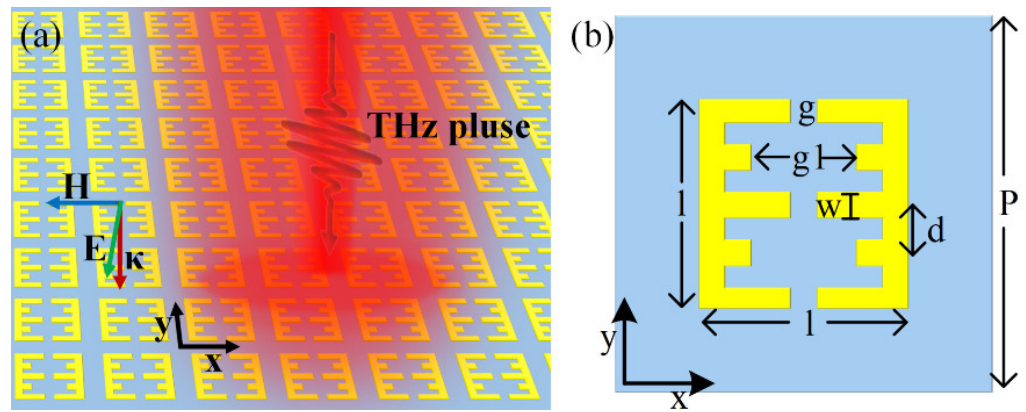


Figure 1. Schematic diagram of the sensor structure. (a) Top view and (b) geometric parameters of the amplification unit cell.

Table 1. Dimensional parameters of the sensor.

Parameters	P	h	l	d	g	w	g1	t
Value/ μm	200	60	40	10	5	5	20	0.2

The transmission spectrum and near-field distribution of the sensor are calculated via the finite element method using a frequency domain solver based on the full-wave electromagnetic simulation software (CST MWS 2020). The infinite periodic array is simulated by setting the x–y plane as a periodic boundary condition and the z direction as an open boundary condition.

3. Results and Discussion

The transmission spectrum of a multi-band sensor operating in the frequency band range of 0.8–1.5 THz is shown in Figure 2. Four narrow-band transmission valleys are observed at $f_1 = 0.996$, $f_2 = 1.214$, $f_3 = 1.333$, and $f_4 = 1.46$ THz, whose transmission intensities are all below 40%. This indicates that the structure can be used as a plasma sensing and filtering device. The quality factor is an important measure of sensor performance that is defined as $Q = f/\text{FWHM}$ (here, f is the central resonance frequency and FWHM is the full-width at half maximum). In this respect, the Q values based on the above resonances of the sensor are found to be 171, 152, 177, and 77, respectively. The larger Q values demonstrate the greater potential of the structure in sensing and detection applications (as a comparison, generally, the Q value is only 10 to 20 [33]).

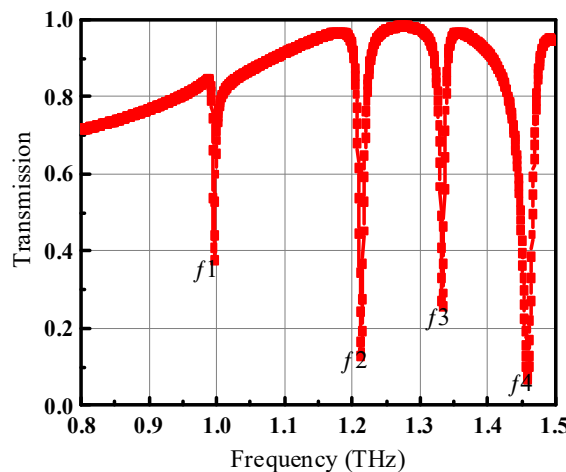


Figure 2. The transmission characteristic curve of the four-band sensor.

Conventional design methods typically superimpose a number of independent metal resonance structures to obtain the multi-band electromagnetic response curves, which may cause various difficulties in the fabrication of sensors, such as high cost, etc. The resonator proposed in the present study possesses a metal groove microstructure to ensure that four-band transmission is implemented. This enables one to simplify the structure design, shorten the structure optimization time, and enrich the response mechanism.

3.1. Analysis of the Resonance Mechanism

In Figure 3, the near-field (with the electric field $\text{Re}\{E_z\}$, and the surface current, $\text{phase} = 0$) distributions of resonance peaks f_1 , f_2 , f_3 , and f_4 are presented to explore the resonance mechanism of the four-band sensor. From Figure 3a1–d1, it is obvious that the electric field in the plane $z = 0$ of the sensor is mainly concentrated in the upper and lower arms of the metal microstructure. The red and blue colors indicate positive and negative values, respectively, from which it can be seen that the four modes all exhibit the dipole resonance, and the local field enhancement is thus achieved. The surface current distributions of each resonance mode are shown in Figure 3a2–d2. The surface currents (as shown by the arrows) are mainly observed on the left and right sides of the metallic microstructure, exhibiting the same distribution along predominately the y -axis direction. The electric dipole (“bright” mode) along the upper and lower arms of the structure, excited by the incident terahertz wave, couples with the magnetic dipole (“dark” mode), which is not directly excited, and forms an asymmetric resonance spectrum. Therefore, we infer that the cause of the resonance is mainly the higher-order Fano resonance [34–37].

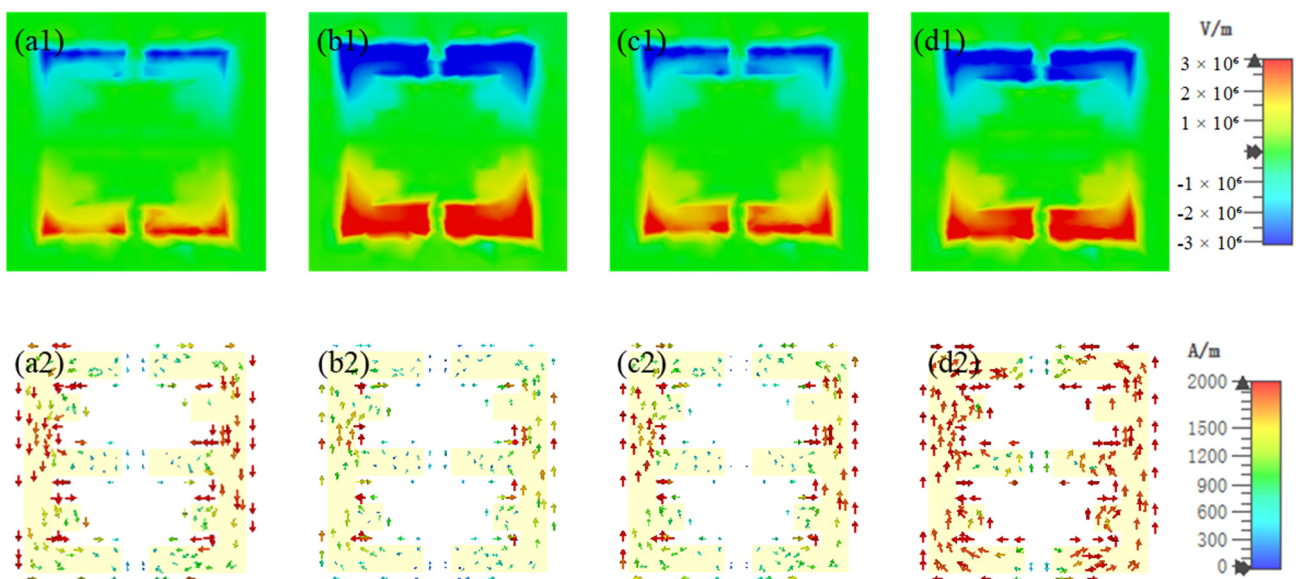


Figure 3. (a1–d1) Electric field distributions of the four-band sensor in the f_1 , f_2 , f_3 , and f_4 modes ($\text{Re}\{E_z$, $z = 0$ plane). (a2–d2) Surface current distributions of the four-band sensor in the f_1 , f_2 , f_3 , and f_4 modes ($z = 0$ plane).

3.2. Analysis of Stability

Figure 4a,b display the effects of polarization angle and incidence angle on the transmission spectrum of the sensor in the case of TE-polarized terahertz waves, respectively. As the polarization angle increases, the resonance frequency of the sensor remains constant and the transmission intensity of f_1 , f_2 , f_3 , and f_4 modes gradually increases. The transmission of the resonance frequency of the sensor is kept below 0.5 for the terahertz waves that are incident at the polarization angles of 0 to 50° . Thus, the designed sensor has good polarization insensitivity characteristics, which decreases the measurement error caused by the improper placement of the device in the actual test to a certain extent. According to Figure 4b, the sensor exhibits the incidence angle dependence. By switching the angle of

incidence from normal to oblique, the four-band resonance mode of the sensor changes to a multi-band mode and the transmission intensity increases compared to that at the normal incidence of the wave. To ensure the validity and accuracy of the results, the sensor should be placed on a smooth carrier table parallel to the direction of the applied electromagnetic field.

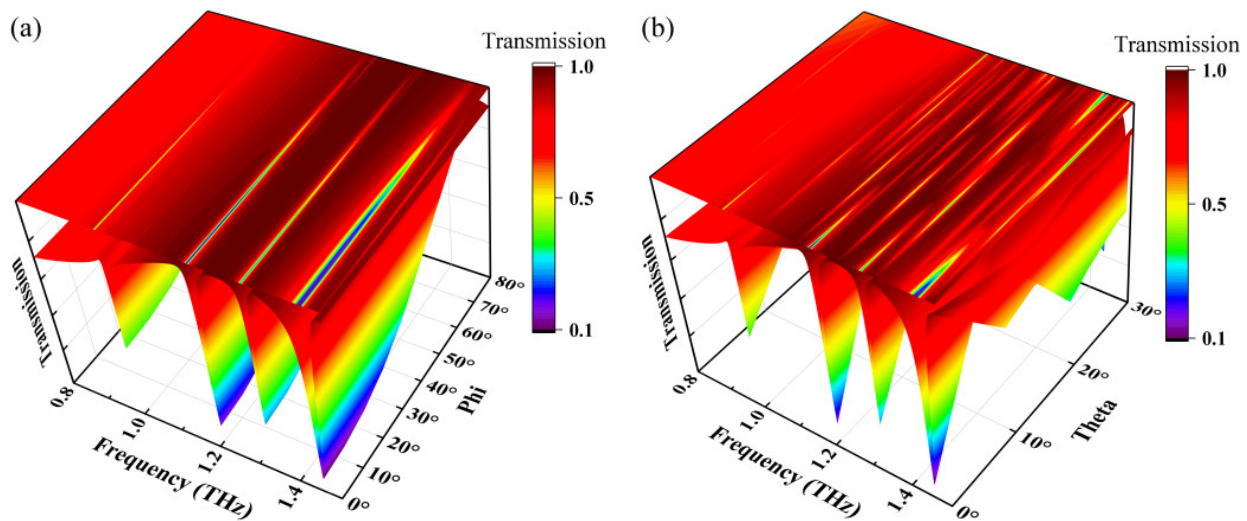


Figure 4. The transmission spectrum of the sensor as a function of (a) polarization angle and (b) angle of incidence.

3.3. Analysis of Sensing Performance

The effective capacitance (C_{eff}) of a sensor depends on the capacitance of the device itself and the capacitance generated by the surrounding medium (the so-called C_{sensor}). Once the structural parameters of the sensor are determined, the capacitance of the device remains almost unchanged. Therefore, the change in the refractive index of the analyte will alter the value of C_{sensor} and thus the resonance characteristics of the sensor (such as resonance frequency, transmission spectrum, etc.). When analyzing the sensing performance of a sensor, analytes with different thicknesses and refractive indices are applied on the sensor's surface. The sensing detection of the analyte to be measured is achieved by monitoring the degree of the resonance frequency shift and the change in transmission.

Sensitivity is a key indicator of the performance of a sensor. The refractive index sensitivity of the sensor is generally calculated as $S = \Delta f / \Delta n$ in GHz/RIU, where Δn indicates the change in the refractive index of the analyte and Δf is the resonance frequency offset. Furthermore, the sensor can be used to measure the thickness of the surface samples, and its sensitivity can thus be found as $S = \Delta f / \Delta h$ in GHz/ μm , where Δh is the change in sample thickness [38,39].

Figure 5a depicts the transmission characteristic curves of the sensor at different thicknesses of the surface analyte. In the simulations, the sample is assumed to be hemoglobin, the refractive index is set at 1.38 (the dielectric losses are neglected) [40,41], and the analyte thickness h_1 varies from 3 to 25 μm . As the thickness of the surface sample increases, all four resonance peaks in the transmission spectrum are red-shifted. Figure 5b presents the frequency of each peak as a function of the thickness of the analyte, where the frequency shifts of the signals increase with the analyte thickness in a roughly linear manner. The thickness sensitivities at the four resonances were calculated to be $S_{f_1} = 0.68$, $S_{f_2} = 1.33$, $S_{f_3} = 1.19$, and $S_{f_4} = 1.91$ GHz/ μm , which can be applied to the thickness measurement of composite materials.

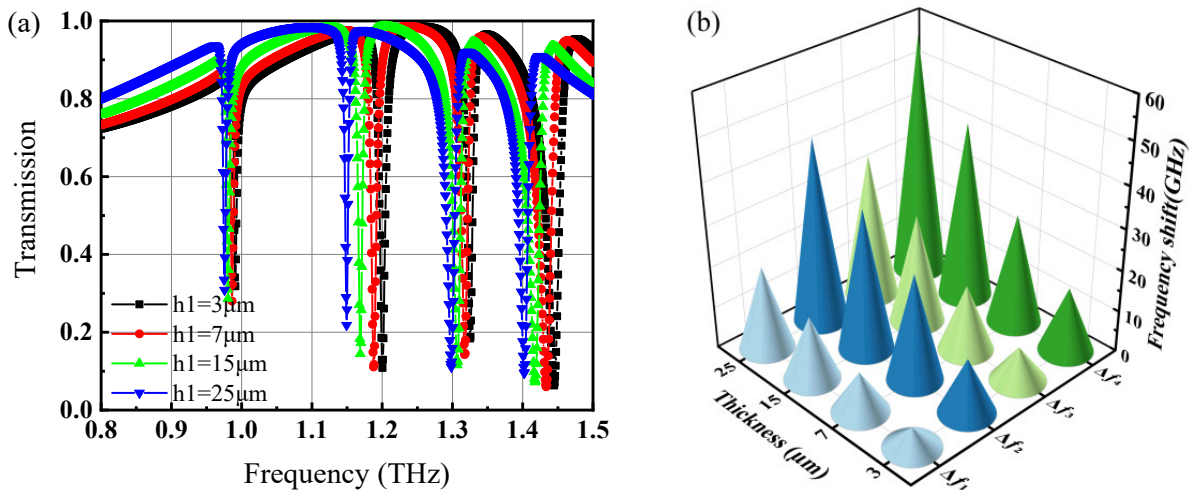


Figure 5. Thickness sensing effect of the sensor: (a) transmission spectrum of the sensor surface covered with analytes of different thicknesses, and (b) resonance sensing signal frequency versus sample thickness.

It can be seen from Figure 5 that the larger the thickness of the analyte, the greater the change in frequency. Hence, the best results are obtained at the analyte thickness of $25 \mu\text{m}$. Since the refractive indices of most substances are in the range of 1.3–1.8 [42], Figure 6a shows the variation of transmission spectra for samples with different refractive indices. As the refractive index of the analyte increases, all four resonance peaks are significantly red-shifted, and the frequency shift increases accordingly. This is due to a significant change in the dielectric constant around the sensor, which is reflected by the shift in resonance frequency. In this respect, Figure 6b visualizes the frequency variation with the refractive index to further analyze the sensor’s refractive index sensitivity. After linear fitting, the refractive index sensitivities at the four resonance peaks are $S_{f_1} = 125$, $S_{f_2} = 106$, $S_{f_3} = 200$, and $S_{f_4} = 104$ GHz/RIU, respectively. In addition, the figure of merit (FOM) is used to characterize the overall performance of the sensor, which is expressed as $\text{FOM} = S/\text{FWHM}$. The FOM values at the four resonance frequencies of the sensor proposed in this paper are $\text{FOM}_{f_1} = 21.5$, $\text{FOM}_{f_2} = 12.8$, $\text{FOM}_{f_3} = 26.7$, and $\text{FOM}_{f_4} = 5.4$, respectively.

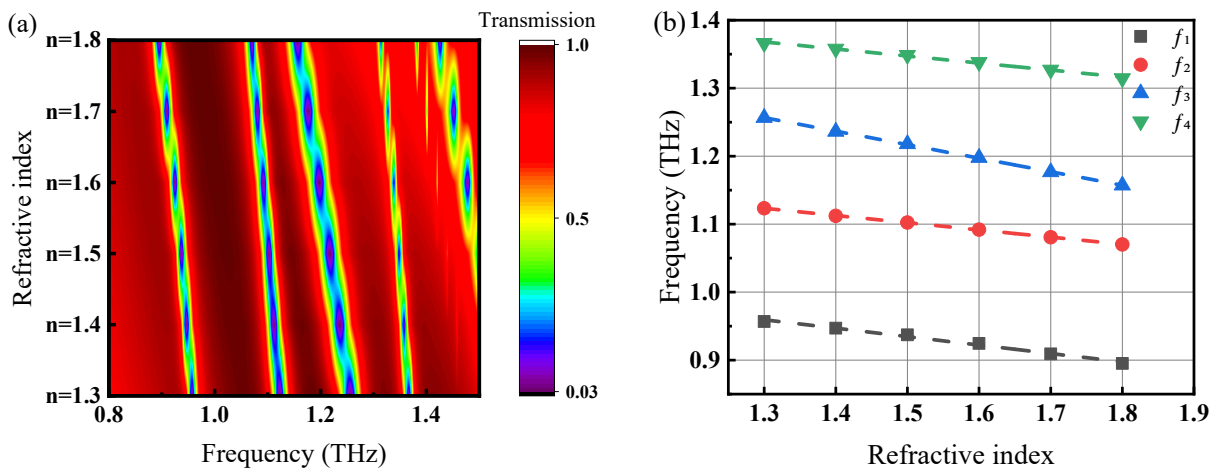


Figure 6. (a) Transmission spectra at $h_1 = 25 \mu\text{m}$ for samples with different refractive indices. (b) Sensing signal frequency versus refractive index for resonance.

Dielectric loss of the analyte is also an essential factor in the variation of the electromagnetic response of the sensor [18]. In particular, the dielectric loss factor, also known as

the angular tangent of dielectric loss ($\tan\delta$), is a parameter that enables one to measure the degree of dielectric loss. Taking the sample with $h_1 = 25 \mu\text{m}$ and $n = 1.38$ as an example, the effect of $\tan\delta$ on the transmission spectrum is further analyzed. As shown in Figure 7 the resonance frequency of the sensor changes less when the value of $\tan\delta$ of the analyte increases. However, the four resonance inclinations gradually increase and the FWHM spreads, resulting in the lower Q values. Therefore, this characteristic makes it easier to distinguish between analytes with different dielectric losses.

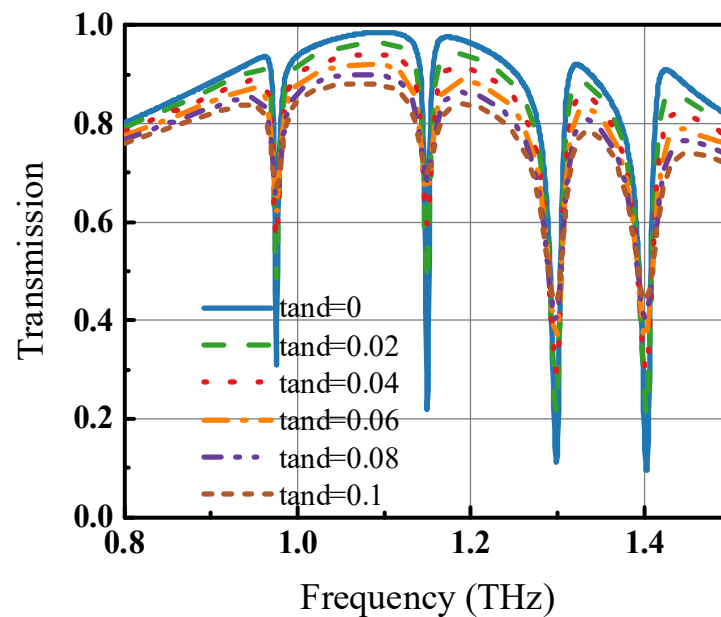


Figure 7. Transmission spectrum of the sensor at various values of $\tan\delta$ of the analyte.

Table 2 shows the performance comparison between the sensors designed in this paper and the reported sensors. The results show that the sensor structure designed in this paper is more prominent in terms of Q-factor, sensitivity, and FOM, which has potential application value in the field of sensing and detection.

Table 2. Comparison of sensor performance.

Reference	Q-Factor	Sensitivity (GHz/RIU)	FOM	Year Published
[29]	-	70	3	2022
[43]	29.94	264	4.46	2021
[44]	44.17	126.0	10.5	2021
[45]	13.76	851	3.16	2022
[46]	50.72	149.5	5.69	2022
This work	177	200	26.7	

The structure designed in this paper is proposed to be prepared by the conventional photolithography technique. The preparation process can be roughly divided into the following steps, as shown in Figure 8. First, a layer of polyimide film with uniform thickness is spin-coated on the silicon substrate, and the metal layer is evaporated on the PI film by an electron beam. Next, a layer of photoresist is applied to the metal film, and the desired metal structure is retained after exposure, development, and etching. Finally, wet etching off all sacrificial layers is carried out to obtain the array structure designed in this paper, i.e., Figure 8h. The slices are preserved according to the desired sample size for use.

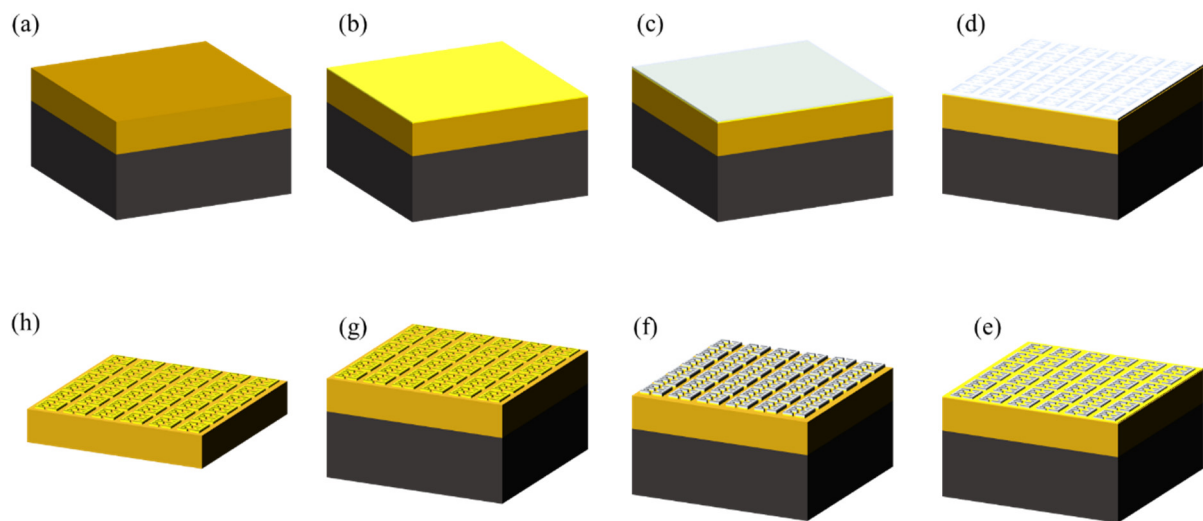


Figure 8. The steps of sensing chip preparation. (a) Spin-coating PI film, (b) gold-plating film, (c) applying photoresist, (d) exposure, (e) development, (f) etching, (g) de-binding, and (h) removal of sacrificial layer.

The Z3 THz-TDS [47] from Zomega was used for the detection of substances and the operating principle is shown in Figure 9. The laser pulses generated by the fiber laser are divided by a beam splitter into a pump beam and a probe beam. The pump beam is passed through a photoconductive antenna to generate the terahertz pulse, which is irradiated on the sensor covering the sample. Then, the pulse carrying the terahertz band information of the sample is converged with the probe beam, and the terahertz time-domain spectral signal of the sample is obtained through the signal processing of terahertz detector devices, delay lines, lock-in amplifiers, etc. Then, the fast Fourier transform is used to obtain the frequency domain signal for subsequent data analysis.

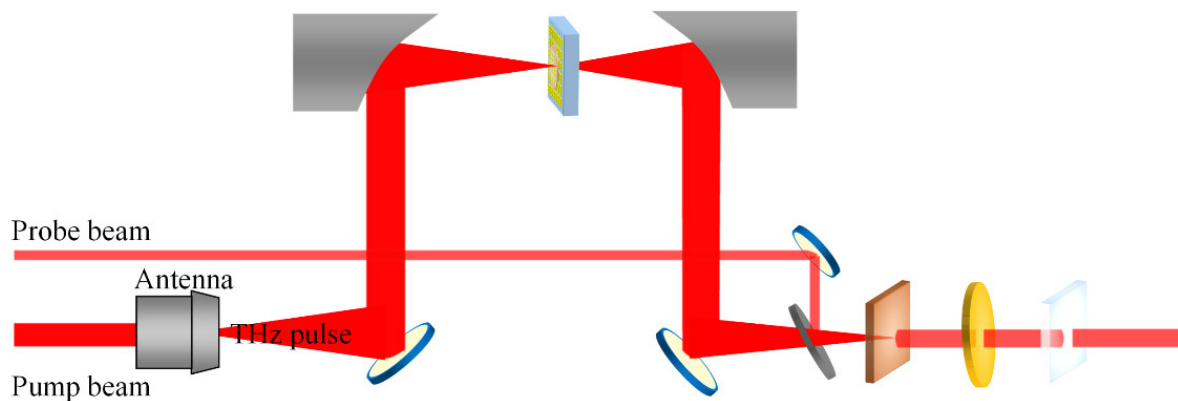


Figure 9. The working principle of THz-TDS.

4. Conclusions

Terahertz metamaterial sensors can reduce the energy propagation speed of light and modulate terahertz waves to enhance the interaction between photons and substances [48,49]. In this paper, a terahertz metamaterial sensor with a metallic notch-type resonator, enabling generation of four resonance modes simultaneously, was proposed. The physical mechanism of the four-band transmission was revealed by analyzing the near-field distribution of resonance peaks in the operating bandwidth of 0.8–1.5 THz, where the dipole resonance dominated at the resonance frequency. The sensor is polarization-insensitive with an angular stability of up to 50°. In addition, the sensor has a high Q value and is capable of sensing changes due to the surrounding medium with refractive

index sensitivity of 200 GHz/RIU and a FOM value up to 26.7. Unlike conventional design strategies for multi-band sensors, the sensor designed in the present study is simple in terms of surface structure design. Such a design solution results in many advantages, among which are shortening the structure optimization time and enriching the design ideas for multi-band terahertz functional devices. Therefore, this work has great significance for enhancing the interaction between terahertz waves and substances and developing state-of-the-art terahertz slow-light devices.

Author Contributions: Conceptualization, H.G.; Data curation, L.L.; Formal analysis, L.L.; Funding acquisition, H.G., Y.J. and Y.Z.; Investigation, G.L., F.W., M.L., X.J. and Z.J.; Methodology, L.L. and H.G.; Project administration, H.G.; Supervision, Z.L. and Y.Z.; Validation, L.L.; Visualization, L.L.; Writing—original draft, L.L.; Writing—review & editing, H.G. All authors have read and agreed to the published version of the manuscript.

Funding: This research was funded by the National Natural Science Foundation of China (61975053, 61705061), the Natural Science Foundation of Henan (222300420040, 202300410111), the Program for Science and Technology Innovation Talents in Universities of Henan Province (22HASTIT017), the Open Fund Project of the Key Laboratory of Grain Information Processing and Control, Ministry of Education, Henan University of Technology (KFJJ2020103), the Major public welfare projects of Henan Province (201300210100), the Innovative Funds Plan of Henan University of Technology (2021ZKCJ04), the Cultivation Program for Young Backbone Teachers in Henan University of Technology, the Key Science and Technology Program of Henan Province of China (222102110246), and the major science and technology project of Henan Province (211110110500).

Institutional Review Board Statement: Not applicable.

Informed Consent Statement: Not applicable.

Data Availability Statement: Data underlying the results presented in this paper are not publicly available at this time but may be obtained from the authors upon reasonable request.

Conflicts of Interest: The authors declare no conflict of interest.

References

1. Lu, W.; Luo, H.; He, L.; Duan, W.; Tao, Y.; Wang, X.; Li, S. Detection of heavy metals in vegetable soil based on THz spectroscopy. *Comput. Electron. Agric.* **2022**, *197*, 106923. [[CrossRef](#)]
2. Cai, J.; Guang, M.; Zhou, J.; Qu, Y.; Xu, H.; Sun, Y.; Xiong, H.; Liu, S.; Chen, X.; Jin, J. Dental caries diagnosis using terahertz spectroscopy and birefringence. *Opt. Express* **2022**, *30*, 13134–13147. [[CrossRef](#)] [[PubMed](#)]
3. Shao, Y.; Zhu, D.; Wang, Y.; Zhu, Z.; Tang, W.; Tian, Z.; Peng, Y.; Zhu, Y. Moxa Wool in Different Purities and Different Growing Years Measured by Terahertz Spectroscopy. *Plant Phenomics* **2022**, *2022*, 9815143. [[CrossRef](#)] [[PubMed](#)]
4. Ueno, Y.; Ajito, K. Analytical Terahertz Spectroscopy. *Anal. Sci. Int. J. Jpn. Soc. Anal. Chem.* **2008**, *24*, 185–192. [[CrossRef](#)]
5. Menikh, A. *Terahertz-Biosensing Technology: Progress, Limitations, and Future Outlook*; Springer: Berlin/Heidelberg, Germany, 2010; Volume 8, pp. 283–295.
6. Shao, Y.; Gu, W.; Qiu, Y.A.; Wang, S.; Peng, Y.; Zhu, Y.; Zhuang, S. Lipids monitoring in *Scenedesmus obliquus* based on terahertz technology. *Biotechnol. Biofuels* **2020**, *13*, 161. [[CrossRef](#)]
7. Im, J.; Goo, T.; Kim, J.; Choi, S.; Hong, S.J.; Bahk, Y.M. Detection of Microplastic in Salts Using Terahertz Time-Domain Spectroscopy. *Sensors* **2021**, *21*, 3161. [[CrossRef](#)]
8. Zhu, Z.; Bian, Y.; Zhang, X.; Zeng, R.; Yang, B. Examination of proline, hydroxyproline and pyroglutamic acid with different polar groups by terahertz spectroscopy. *Spectrochim. Acta Part A Mol. Biomol. Spectrosc.* **2022**, *267*, 120539. [[CrossRef](#)]
9. Lee, J.; Kim, S. Quantitative Analysis of Monosaccharide Concentration Using Terahertz Time-Domain Spectroscopy in Ambient Atmosphere. *IEEE Trans. Instrum. Meas.* **2021**, *70*, 1–8. [[CrossRef](#)]
10. Jiang, Y.; Ge, H.; Zhang, Y. Quantitative analysis of wheat maltose by combined terahertz spectroscopy and imaging based on Boosting ensemble learning. *Food Chem.* **2020**, *307*, 125533. [[CrossRef](#)]
11. Shi, J.; Li, Z.; Sang, D.K.; Xiang, Y.; Li, J.; Zhang, S.; Zhang, H. THz photonics in two dimensional materials and metamaterials: Properties, devices and prospects. *J. Mater. Chem. C* **2018**, *6*, 1291–1306. [[CrossRef](#)]
12. Lee, S.; Baek, S.; Kim, T.T.; Cho, H.; Lee, S.; Kang, J.H.; Min, B. Metamaterials for Enhanced Optical Responses and their Application to Active Control of Terahertz Waves. *Adv. Mater.* **2020**, *32*, e2000250. [[CrossRef](#)] [[PubMed](#)]
13. Zhang, Y.; Zhao, Y.; Liang, S.; Zhang, B.; Wang, L.; Zhou, T.; Kou, W.; Lan, F.; Zeng, H.; Han, J.; et al. Large phase modulation of THz wave via an enhanced resonant active HEMT metasurface. *Nanophotonics* **2018**, *8*, 153–170. [[CrossRef](#)]
14. Sensale-Rodriguez, B.; Yan, R.; Kelly, M.M.; Fang, T.; Tahy, K.; Hwang, W.S.; Jena, D.; Liu, L.; Xing, H.G. Broadband graphene terahertz modulators enabled by intraband transitions. *Nat. Commun.* **2012**, *3*, 780. [[CrossRef](#)] [[PubMed](#)]

15. Zhao, H.; Chen, X.; Ouyang, C.; Wang, H.; Kong, D.; Yang, P.; Zhang, B.; Wang, C.; Wei, G.; Nie, T.; et al. Generation and manipulation of chiral terahertz waves in the three-dimensional topological insulator Bi_2Te_3 . *Adv. Photonics* **2020**, *2*, 62–70. [[CrossRef](#)]
16. Yang, J.; Qi, L.; Li, B.; Wu, L.; Shi, D.; Ahmed Uqaili, J.; Tao, X. A terahertz metamaterial sensor used for distinguishing glucose concentration. *Results Phys.* **2021**, *26*, 104332. [[CrossRef](#)]
17. Yan, X.; Yang, M.; Zhang, Z.; Liang, L.; Wei, D.; Wang, M.; Zhang, M.; Wang, T.; Liu, L.; Xie, J.; et al. The terahertz electromagnetically induced transparency-like metamaterials for sensitive biosensors in the detection of cancer cells. *Biosens. Bioelectron.* **2018**, *126*, 485–492. [[CrossRef](#)]
18. Zhang, C.; Xue, T.; Zhang, J.; Liu, L.; Xie, J.; Wang, G.; Yao, J.; Zhu, W.; Ye, X. Terahertz toroidal metasurface biosensor for sensitive distinction of lung cancer cells. *Nanophotonics* **2022**, *11*, 101–109. [[CrossRef](#)]
19. Cheng, R.; Xu, L.; Yu, X.; Zou, L.; Shen, Y.; Deng, X. High-sensitivity biosensor for identification of protein based on terahertz Fano resonance metasurfaces. *Opt. Commun.* **2020**, *473*, 125850. [[CrossRef](#)]
20. Wang, G.; Zhu, F.; Lang, T.; Liu, J.; Hong, Z.; Qin, J. All-metal terahertz metamaterial biosensor for protein detection. *Nanoscale Res. Lett.* **2021**, *16*, 109. [[CrossRef](#)]
21. Jin, Z.A.; Ning, M.; Lld, E.; Jx, E.; Hua, F.; Jy, D.; Tcb, C.; Wz, A. Highly Sensitive Detection of Malignant Glioma Cells Using Metamaterial-inspired THz Biosensor based on Electromagnetically Induced Transparency. *Biosens. Bioelectron.* **2021**, *185*, 113241.
22. Xiaoxue, D.; Xiaodong, Z.; Yafei, W.; Guoxin, M.; Yong, L.; Bin, W.; Hanping, M. Highly sensitive detection of plant growth regulators by using terahertz time-domain spectroscopy combined with metamaterials. *Opt. Express* **2021**, *29*, 36535–36545.
23. Zhang, H.; Li, Z.; Hu, F.; Qin, B.; Zhao, Y.; Chen, T.; Hu, C. Sensitive distinction between herbs by terahertz spectroscopy and a metamaterial resonator. *Spectrosc. Lett.* **2018**, *51*, 174–178. [[CrossRef](#)]
24. Khwanchai, T.; Habibe, D. Herbicide/pesticide sensing with metamaterial absorber in THz regime. *Sens. Actuators A Phys.* **2021**, *331*, 112960.
25. Zhang, Y.; Yixing, Z.; Yunxia, Y.; Xiaoxian, S.; Maosheng, Y.; Yunpeng, R.; Xudong, R.; Lanju, L.; Jianquan, Y. High-sensitivity detection of chlorothalonil via terahertz metasensor. *Mater. Res. Express* **2020**, *7*, 095801. [[CrossRef](#)]
26. Chen, Z.; Qu, F.; Wang, Y.; Nie, P. Terahertz dual-band metamaterial absorber for trace indole-3-acetic acid and tricyclazole molecular detection based on spectral response analysis. *Spectrochim. Acta Part A Mol. Biomol. Spectrosc.* **2021**, *263*, 120222. [[CrossRef](#)] [[PubMed](#)]
27. Xu, J.; Liao, D.; Gupta, M.; Zhu, Y.; Zhuang, S.; Singh, R.; Chen, L. Terahertz Microfluidic Sensing with Dual-Torus Toroidal Metasurfaces. *Adv. Opt. Mater.* **2021**, *9*, 2100024. [[CrossRef](#)]
28. Li, F.; He, K.; Tang, T.; Mao, Y.; Wang, R.; Li, C.; Shen, J. The terahertz metamaterials for sensitive biosensors in the detection of ethanol solutions. *Opt. Commun.* **2020**, *475*, 126287. [[CrossRef](#)]
29. Yao, H.; Mei, H.; Zhang, W.; Zhong, S.; Wang, X. Theoretical and Experimental Research on Terahertz Metamaterial Sensor With Flexible Substrate. *IEEE Photonics J.* **2022**, *14*, 1–9. [[CrossRef](#)]
30. Chen, T.; Jiang, W.; Yin, X. Dual-Band Ultrasensitive Terahertz Sensor Based on Tunable Graphene Metamaterial Absorber. *Superlattices Microstruct.* **2021**, *154*, 106898. [[CrossRef](#)]
31. Ma, A.; Zhong, R.; Wu, Z.; Wang, Y.; Yang, L.; Liang, Z.; Fang, Z.; Liu, S. Ultrasensitive THz Sensor Based on Centrosymmetric F-Shaped Metamaterial Resonators. *Front. Phys.* **2020**, *8*, 584630. [[CrossRef](#)]
32. Veeraselvam, A.; Mohammed, G.N.A.; Savarimuthu, K.; Vijayaraman, P.D. An Ultra-Thin Multiband Refractive Index-Based Carcinoma Sensor Using THz Radiation. *IEEE Sens. J.* **2022**, *22*, 2045–2052. [[CrossRef](#)]
33. Fang, X.; Xiong, L.; Shi, J.; Ding, H.; Li, G. Narrow quadrupolar surface lattice resonances and band reversal in vertical metal-insulator-metal gratings. *J. Phys. D Appl. Phys.* **2021**, *55*, 025111. [[CrossRef](#)]
34. Chen, X.; Fan, W. Ultrasensitive terahertz metamaterial sensor based on spoof surface plasmon. *Sci. Rep.* **2017**, *7*, 2092. [[CrossRef](#)] [[PubMed](#)]
35. Ma, C.; Yan, J.; Huang, Y.; Yang, G. Directional Fano resonance in an individual GaAs nanospheroid. *Small* **2019**, *15*, 1900546. [[CrossRef](#)] [[PubMed](#)]
36. Chen, L.; Wei, Y.; Zang, X.; Zhu, Y.; Zhuang, S. Excitation of dark multipolar plasmonic resonances at terahertz frequencies. *Sci. Rep.* **2016**, *6*, 22027. [[CrossRef](#)] [[PubMed](#)]
37. Born, N.; Al-Naib, I.; Jansen, C.; Ozaki, T.; Morandotti, R.; Koch, M. Excitation of multiple trapped-eigenmodes in terahertz metamolecule lattices. *Appl. Phys. Lett.* **2014**, *104*, 101107. [[CrossRef](#)]
38. Srivastava, Y.K.; Ako, R.T.; Gupta, M.; Bhaskaran, M.; Sriram, S.; Singh, R. Terahertz sensing of 7 nm dielectric film with bound states in the continuum metasurfaces. *Appl. Phys. Lett.* **2019**, *115*, 151105. [[CrossRef](#)]
39. Karmakar, S.; Kumar, D.; Varshney, R.K.; Chowdhury, D.R. Strong terahertz matter interaction induced ultrasensitive sensing in Fano cavity based stacked metamaterials. *J. Phys. D Appl. Phys.* **2020**, *53*, 415101. [[CrossRef](#)]
40. Veeraselvam, A.; Mohammed, G.N.A.; Savarimuthu, K. A Novel Ultra-Miniaturized Highly Sensitive Refractive Index-Based Terahertz Biosensor. *J. Light. Technol.* **2021**, *39*, 7281–7287. [[CrossRef](#)]
41. Sharma, P.; Sharan, P. Design of photonic crystal based ring resonator for detection of different blood constituents. *Opt. Commun.* **2015**, *348*, 19–23. [[CrossRef](#)]
42. Veeraselvam, A.; Mohammed, G.N.A.; Savarimuthu, K.; Sankararajan, R. A novel multi-band biomedical sensor for THz regime. *Opt. Quantum Electron.* **2021**, *53*, 354. [[CrossRef](#)]

43. Sun, R.; Li, W.; Meng, T.; Zhao, G. Design and optimization of terahertz metamaterial sensor with high sensing performance. *Opt. Commun.* **2021**, *494*, 127051. [[CrossRef](#)]
44. Xiong, Z.; Shang, L.; Yang, J.; Chen, L.; Guo, J.; Liu, Q.; Danso, S.A.; Li, G. Terahertz sensor with resonance enhancement based on square split-ring resonators. *IEEE Access* **2021**, *9*, 59211–59221. [[CrossRef](#)]
45. Nickpay, M.-R.; Danaie, M.; Shahzadi, A. Highly sensitive THz refractive index sensor based on folded split-ring metamaterial graphene resonators. *Plasmonics* **2022**, *17*, 237–248. [[CrossRef](#)]
46. Abdulkarim, Y.I.; Xiao, M.; Awl, H.N.; Muhammadsharif, F.F.; Lang, T.; Saeed, S.R.; Alkurt, F.Ö.; Bakır, M.; Karaaslan, M.; Dong, J. Simulation and lithographic fabrication of a triple band terahertz metamaterial absorber coated on flexible polyethylene terephthalate substrate. *Opt. Mater. Express* **2022**, *12*, 338–359. [[CrossRef](#)]
47. Jiang, Y.; Li, G.; Ge, H.; Wang, F.; Li, L.; Chen, X.; Lv, M.; Zhang, Y. Adaptive compressed sensing algorithm for terahertz spectral image reconstruction based on residual learning. *Spectrochim. Acta Part A Mol. Biomol. Spectrosc.* **2022**, *281*, 121586. [[CrossRef](#)]
48. Baba, T. Slow light in photonic crystals. *Nat. Photonics* **2008**, *2*, 465–473. [[CrossRef](#)]
49. Bandurin, D.; Mönch, E.; Kapralov, K.; Phinney, I.; Lindner, K.; Liu, S.; Edgar, J.; Dmitriev, I.; Jarillo-Herrero, P.; Svintsov, D. Cyclotron resonance overtones and near-field magnetoabsorption via terahertz Bernstein modes in graphene. *Nat. Phys.* **2022**, *18*, 462–467. [[CrossRef](#)]